





Breaking wave impacts on an elastic plate

Zhengyu Hu¹  and Yuzhu Pearl Li¹ 

¹Department of Civil and Environmental Engineering, National University of Singapore, Singapore 117576, Republic of Singapore

Corresponding author: Yuzhu Pearl Li, pearl.li@nus.edu.sg

(Received 14 August 2024; revised 18 June 2025; accepted 20 June 2025)

Breaking wave impacts on rigid structures have been extensively studied, yet the role of structural elasticity in shaping the impact and response remains insufficiently understood. In this study, we experimentally investigate the hydroelastic behaviour of a vertical cantilever plate subjected to multimodal solitary breaking wave impacts. The plate is mounted near the still water level on a 1 : 10 sloping beach, and the wave height-to-depth ratio (H/h) is varied from 0.15 to 0.40 to systematically control the impact type from non-breaking to highly aerated wave impacts. We show that aeration significantly affects hydroelastic impacts. The spatio-temporal extent of the impact pressure on the elastic plate increases with air entrapment, while the peak pressure becomes highly sensitive as the wave approaches the flip-through regime. Pressure oscillations associated with bubble formation induce high-frequency structural vibrations, particularly under low-aeration conditions. Furthermore, we find that the elasticity has a limited effect on the peak pressure, impact duration and impulse, but increases the maximum quasi-hydrostatic force on the plate for the scenarios investigated. Following the impact, two distinct free-top deflections are identified, i.e. a deflection Δx_{imp} with high acceleration induced by the impact pressure and a deflection Δx_{hp} with high magnitude caused by the maximum quasi-hydrostatic pressure. These deflections scale with the Cauchy number as $\Delta x_{imp}/l \sim Ca_{imp}/6$ and $\Delta x_{hp}/l \sim Ca_{hp}/12$ (where l is the plate length), exhibiting parabolic and linear trends with H/h , respectively. This work presents a benchmark dataset and introduces a predictive law for structural deflection, providing practical insights into hydroelastic effects across various impact regimes.

Key words: surface gravity waves, wave breaking, wave-structure interactions

1. Introduction

Breaking wave impacts, often referred to as slamming, present significant challenges in maritime and coastal engineering due to their sudden, extreme loading over short durations (Faltinsen & Timokha 2009; Dias & Ghidaglia 2018). These violent events can inflict severe damage on various marine and coastal structures, including liquefied natural gas carriers, flexible wave barriers, wave energy converters, monopile-supported offshore structures and coastal infrastructure (Oumeraci 1994; Faltinsen & Timokha 2009; Kapsenberg 2011; Tiron *et al.* 2015; Wei *et al.* 2016). In shipbuilding, such impacts can induce a whipping response in the hull, compromising structural integrity (Dias & Ghidaglia 2018). Along coastlines, breaking waves contribute to hydraulic fractures in cliffs and the transport of clifftop boulders, playing a crucial role in shaping coastal geomorphology (Herterich, Cox & Dias 2018; Thompson, Young & Dickson 2019; Kennedy, Cox & Dias 2021).

Breaking waves are primarily initiated by reducing water depth (Peregrine 1983; Li, Larsen & Fuhrman 2022), focusing components with different frequencies (Banner & Peregrine 1993) or modulational instability (Melville 1982; Li & Fuhrman 2021), leading to dramatic surface changes and air entrainment (Deane & Stokes 2002; Deike, Melville & Popinet 2016). Numerous studies have attempted to characterise the impulsive pressure induced by the impact of breaking waves on rigid objects. Although impulses derived from integrating pressures over the impact duration exhibit high repeatability (Cooke & Peregrine 1995), variations in the breaking crest shape prior to impact primarily contribute to the stochastic variability of impact modes. This results in substantial differences in pressure between breaking events, even for nominally identical waves (Bullock *et al.* 2007; Raby *et al.* 2022; Moalemi *et al.* 2024). To better characterise these variations, primary types of the breaking wave impact are classified based on breaking wave shape (see figure 1), impact pressure characteristics and evidence of air entrapment. Slightly breaking wave impact represents a transition from unbroken to fully developed impacts (Bullock *et al.* 2007), where the run-up jet forms before the wave crest arrives, preventing direct wave collision. The peak impact pressure typically ranges from 1.0 to 2.5 times the maximum quasi-hydrostatic pressure. In particular, flip-through impact occurs when the run-up jet and the wave crest converge at a common impact point (Peregrine 2003; Moalemi *et al.* 2024). Rapid focusing of the wave free surface can result in spatially and temporally localised impact pressures (Chan & Melville 1988) and a vertical jet with accelerations up to 1500g (Lugni, Brocchini & Faltinsen 2006), where g is the gravitational acceleration. When the wave front is overturning, low aeration and high aeration occur, characterised by relatively little and significant air entrapment between the water and the structure, respectively. The boundary between flip-through and overturning impacts lies in whether the wave crest strikes the wall. Numerical simulations by Cooke & Peregrine (1990) and experiments by Chan & Melville (1988) indicated that the largest pressure arises under the flip-through impact. However, subsequent studies have shown that the highest impact pressure is more likely to occur when a tiny air pocket becomes trapped between a nearly vertical or slightly curled wave front and the wall (Bagnold 1939; Hattori, Arami & Yui 1994; Bredmose, Peregrine & Bullock 2009; Jensen 2019), or when a large air pocket is engulfed by a plunging breaker (Hull & Müller 2002; Hu & Li 2023). Therefore, the flip-through condition does not necessarily produce the most extreme pressure peaks. The aerated impact is typically accompanied by pressure oscillations caused by the alternating compression and expansion of air pockets (Hattori *et al.* 1994), with negative (sub-atmospheric) pressures occurring in extreme circumstances (Bullock *et al.* 2007; Bredmose *et al.* 2009; Hu & Li 2023). The frequency of pressure oscillations increases with the decreased trapped air (Hattori *et al.* 1994). In their experimental investigations

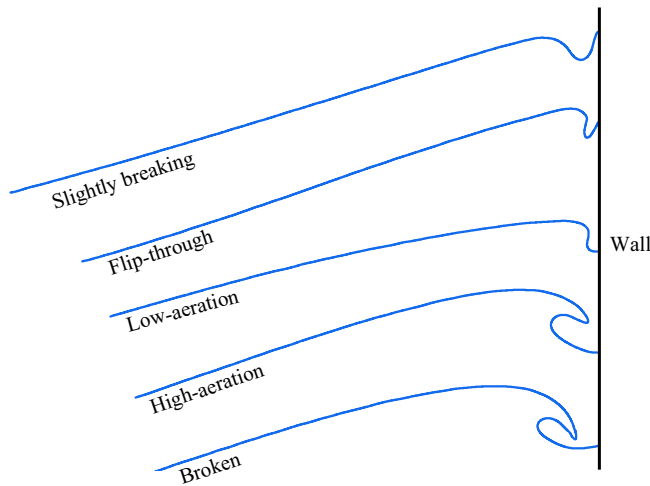


Figure 1. Schematic representation of breaking wave shape for main impact types.

of the impact of a deep-water plunging breaker, Wang *et al.* (2018) estimated the bubble size by the frequency of pressure oscillations. This estimation relies on the relationship between the natural frequency of a spherical bubble in water and its equilibrium radius (Plesset & Prosperetti 1977). In the presence of wall boundary effects, Topliss, Cooker & Peregrine (1992) derived a theoretical expression for the natural frequency of a single two-dimensional gas pocket with a semicircular cross-section against a vertical wall. However, pressure oscillations are not always related to bubble oscillations but also to excited structural vibrations. Moalemi *et al.* (2024) showed that, in the absence of bubbles, the vibration of a monopile can lead to alternative positive and negative pressures. When the incoming wave has already broken before reaching the structure, it generates an aerated and turbulent bore, resulting in a broken wave impact (Bullock *et al.* 2007). The impact pressures are generally lower than those of overturning impacts but can have longer durations.

Lafeber, Bogaert & Brosset (2012a,b) introduced three elementary loading processes (ELPs) to characterise the impact-induced loading processes. The direct impact ELP1 is identified when a solid abruptly halts a fluid, exhibiting nearly discontinuous velocities at the point of contact. The building jet ELP2 represents the most common loading process, characterized by fluid run-up or drawdown along the wall. The compression of entrapped or escaping air ELP3 is characterised by the oscillating air enclosure at a relatively low frequency. Various combinations of ELPs may arise during an isolated breaking wave impact event (Dias & Ghidaglia 2018). Most studies on the impact have been concentrated on a small scale. Bredmose, Bullock & Hogg (2015) analytically and numerically investigated the effects of scale on violent breaking wave impacts. They concluded that most impact types are generally scalable by the Froude scaling law. However, low-aeration and high-aeration impacts should follow the Bagnold–Mitsuyasu scaling law when their maximum pressures exceed 318 kPa.

Additional aspects of breaking wave impact, including the effects of initial air entrainment (Peregrine & Thais 1996; Bredmose *et al.* 2015), inclined contact surface (Bullock *et al.* 2007; Qing, Liu & Guo 2024), wave front perturbation (van Meerkerk *et al.* 2022; Moalemi *et al.* 2024) and boiling liquid (Ezeta *et al.* 2025) have also been investigated, particularly concerning impact loads on the rigid wall and monopile (Li & Fuhrman 2022). Steer, Kimmoun & Dias (2021) conducted laboratory experiments to investigate the displacements of a movable clifftop boulder caused by breaking wave

impacts. The largest displacements occurred when high pressures combined with long impact durations, particularly under near flip-through impact conditions. Hydroelasticity (interaction between fluids and flexible structures) frequently occurs during violent impact events in various applications and across all ELPs (Faltinsen 2000; Dias & Ghidaglia 2018; Hu, Huang & Li 2023). Although several numerical studies (Ten, Malenica & Korobkin 2011; Sriram & Ma 2012; Hu & Li 2023) have explored hydroelastic impacts, experimental investigations remain limited. Kimmoun, Malenica & Socolan (2009) provided a dataset of pressure and structural deflections for a flexible plate subjected to high-aeration wave impacts, showing that the induced vibrations align closely with the first natural mode of the plate. Mai *et al.* (2020) conducted plate drop and wave impact tests, demonstrating that structural elasticity significantly reduces hydrodynamic impact loads. Shen *et al.* (2024) examined hydroelastic effects during flip-through impacts in a nearly two-dimensional (2-D) rectangular tank, highlighting how impact impulse and duration vary with material elasticity. Despite these efforts, the response of deformable structures to multimodal breaking wave impacts and their influence on impact characteristics remain poorly understood. As noted by Dias & Ghidaglia (2018), elastic effects in violent breaking wave impacts remain an open research challenge. Coastal and offshore structures experience complex loading conditions that involve both impulsive and quasi-hydrostatic phases, yet most existing studies focus on rigid structures. The extent to which structural flexibility modifies impact pressures and structural responses has not been systematically investigated across different breaking wave impact conditions, highlighting the need for further experimental research.

To address this gap, we conduct a set of controlled laboratory experiments on a vertical cantilever plate subjected to repeated, isolated and multimodal breaking wave impacts. This study provides the first detailed dataset capturing the transition between impulsive and quasi-hydrostatic loading in hydroelastic wave–structure interactions, serving as a benchmark for numerical model validation. The remainder of the paper is organised as follows. Section 2 describes the experimental details, including set-up, instrumentation, procedure and data analysis techniques. Section 3 presents the spatio-temporal variations of wave surface profile, pressure distribution and structural response induced by distinctive impacts. Furthermore, we analyse how elasticity influences key impact parameters, such as pressure magnitude, impact duration, impulse and quasi-hydrostatic loading. Building on these insights, we propose and validate a simple predictive law for maximum plate deflection, offering a practical estimation approach for flexible structures subjected to breaking wave impacts. Finally, conclusions are drawn in § 4.

2. Methodology

The 1 : 50 scaled laboratory experiments are conducted in a wave flume at the Hydraulic Engineering Laboratory, National University of Singapore. The experimental details are presented in §§ 2.1–2.3, and the time series analysis of impact pressure is shown in § 2.4.

2.1. Experimental set-up and wave conditions

The wave flume (38 m long, 0.9 m wide and 0.9 m high) is equipped with a 5-m long-stroke piston-type wavemaker at one end and a glass plane beach with a 1 : 10 slope at the other, as sketched in figure 2(a). A vertical cantilever plate made of polymethyl methacrylate (PMMA) is mounted on the beach, with its fixed end positioned near the still water level. The cantilever plate configuration was chosen to isolate the hydroelastic response under breaking wave impacts while ensuring a well-defined, reproducible boundary condition. This set-up allows direct measurement of structural deflections and strains without the

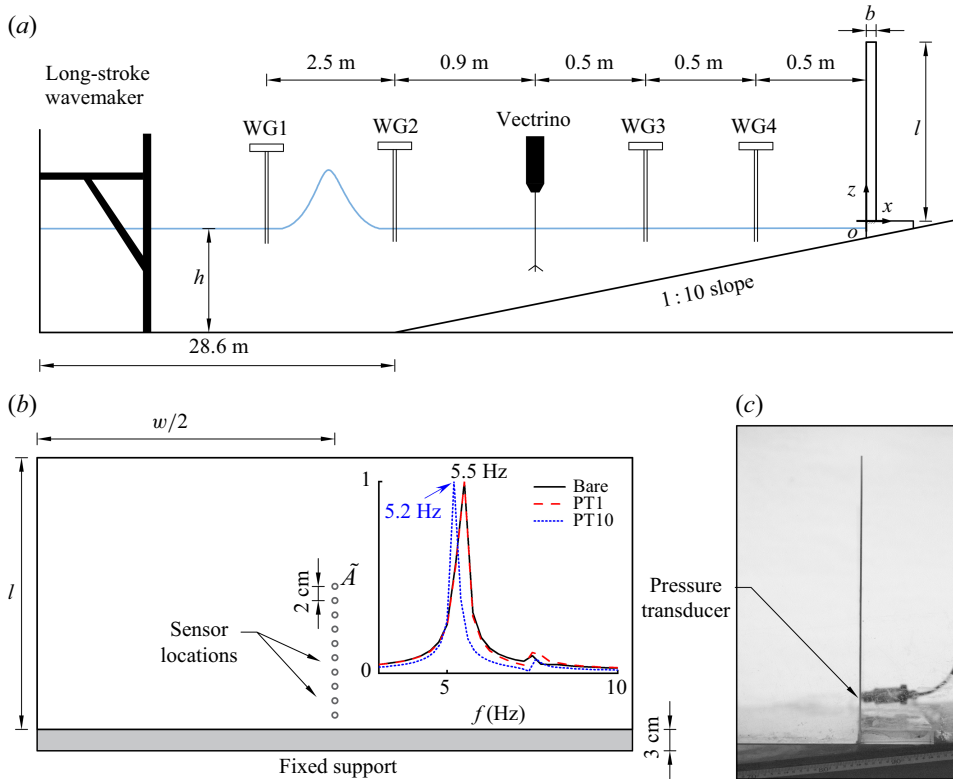


Figure 2. Experimental set-up (not to scale). (a) Wave flume, vertical plate and instrumentation. (b) Front view of the plate, with the array of circles indicating pressure measurement points. The inset displays the amplitude spectrum of the free vibration response from the impact hammer test, where \tilde{A} represents the normalised amplitude and f denotes the frequency. (c) Side view of the elastic plate with PT1 mounted.

complexity of additional support reactions. Cantilevered structures are relevant in marine and coastal engineering, including flexible wave barriers and deformable wave energy converters (Faltinsen & Timokha 2009). Similar cantilever-like behaviour can also be observed in coastal cliffs and overhanging structures subject to wave impact (Herterich *et al.* 2018; Thompson *et al.* 2019). While real-world conditions may differ, this set-up provides a fundamental basis for studying hydroelastic interactions, with findings extendable to more complex configurations through numerical and experimental studies. The Cartesian coordinate system is defined with the x -axis pointing toward the onshore direction and the z -axis oriented vertically. The coordinate origin (o) is located at the toe of the plate. The elastic plate, mounted on a fixed PMMA support 0.03 m from the beach, has a length l of 0.38 m, width w of 0.895 m and thickness b of 0.003 m, as shown in figure 2(b). The Young's modulus E and density ρ_s of the plate are 3.2 GPa and 1190 kg m⁻³, respectively. The plate dimension and material properties are provided by the manufacturer and verified by our measurement. The natural frequency of the first mode in vacuo is $f_n = k_n / 2\pi \sqrt{EI / \rho_s b l^4} = 5.5$ Hz, where $I = b^3 / 12$ is the moment of inertia and $k_n = 3.52$ under 2-D assumptions (Young, Budynas & Sadegh 2012). This theoretical value was validated through an impact hammer test conducted on the bare plate under dry conditions. The 0.02 m-thick plate functions as a rigid group, with negligible deformations.

Multiple wave conditions (each containing a single wave crest) are performed for detailed breaking wave impact and corresponding structural response investigations. The

Test no.	Impact type	H/h	S_0	β	L_w/l_a	Ca_{imp}	Ca_{hp}
1	Unbroken	0.15	0.393	—	—	0.000	0.054
2	Slightly breaking	0.20	0.340	0.34π	—	0.011	0.273
3	Slightly breaking	0.25	0.304	0.27π	—	0.037	0.473
4	Low aeration	0.30	0.278	—	1.33	0.162	0.783
5	Low aeration	0.33	0.265	—	1.70	0.306	1.145
6	High aeration	0.35	0.257	—	1.39	0.462	1.336
7	High aeration	0.40	0.240	—	1.30	0.661	1.720

Table 1. Summary of all test conditions representing different breaking wave impact regimes. Here, H and h denote the initial offshore wave height and water depth, respectively, S_0 is the beach slope parameter, β is the effective deadrise angle of the impacting wave front, L_w is the length of the water column compressing the entrapped air, l_a is the mean initial thickness of the air cushion and Ca_{imp} and Ca_{hp} are the Cauchy numbers characterising the impulsive and quasi-hydrostatic loading phases, respectively. The variables are discussed in more detail in the main text where they are first introduced.

solitary wave is generated using Grimshaw's third-order analytical solution (Grimshaw 1971) for the free surface profile. The wave undergoes shoaling on the sloping beach to achieve a single breaking crest before interacting with the vertical plate. Seven solitary wave conditions corresponding to four main impact types representing unbroken, slightly breaking, low-aeration and high-aeration impacts are examined, as listed in table 1. The ratio of the initial offshore wave height H to the water depth h ranges from 0.15 to 0.40, while the beach slope parameter $S_0 = 1.521S/\sqrt{H/h}$ (S being the beach slope), which characterises the breaker type for solitary waves (Grilli, Svendsen & Subramanya 1997), varies from 0.393 to 0.240. The demarcation of distinctive breaking wave impacts is based on the pressure characteristics and air entrapment evidence (Bullock *et al.* 2007). Boundaries in H/h are established to separate impact types via extensive tests using the pressure history recorded by the pressure transducer and breaking wave shape captured by the high-speed movie recordings. The constant offshore water depth $h = 0.26$ m is used in all tests.

2.2. Instrumentation

To capture the wave surface elevation during propagation, four capacitance wave gauges (WGs) are positioned at $x = -4.9, -2.4, -1.0$ and -0.5 m along the flume, as illustrated in figure 2(a). The WGs have an accuracy of 1 mm, corresponding to approximately 2.5 % of the lowest prescribed wave height. Although this may introduce minor uncertainties, the influence on the overall results is negligible. Most test cases involve larger waves, for which this accuracy represents only a small fraction of the measured wave height. The sampling rate of WGs is 200 Hz. The Nortek Vectrino (acoustic Doppler velocimeter) at a sampling rate of 200 Hz is installed at $x = -1.5$ m to measure the flow velocity profile. The Vectrino measurements range from $z/h_c = 0.06$ to 0.66 with an interval of 0.06, where h_c is the local water depth. The seeding material provided with the Vectrino is carefully added to ensure sufficient scattering of acoustic signals for reliable measurements before each test. During the experiment, the signal-to-noise ratio is greater than 21.5 on average. The time history of the pressure on the plate is recorded by the ATM.1ST precision pressure transducer (PT) at a sampling rate of 20 kHz. The accuracy is 0.1 % full scale, and the response time is less than 1 ms. The full-scale range of the sensor is 30 psi, meaning the maximum uncertainty in pressure measurements is ± 0.03 psi. This translates to an approximate accuracy of ± 15 psi when interpreted at the prototype scale, assuming Froude scaling, based on a representative 1 : 50 scale commonly used for coastal

and offshore structures. The measuring diaphragm of the PT is a circle with a diameter of 4 mm. Ten measurement points PT1–PT10 at 2–20 cm from the plate bottom with an interval of 2 cm are set to cover the wave impact region, see [figure 2\(b\)](#). The PT is securely mounted into pre-drilled holes in the plate, precisely sized to match its process connection port. This design ensures a stable and firm fit without requiring additional bulkheads or spacers, maintaining accurate pressure measurements and structural integrity. To evaluate the influence of a mounted PT on the material properties of the elastic plate, a hammer test is conducted. The results reveal a maximum reduction in the natural frequency from 5.5 (bare plate) to 5.2 Hz with PT10 installed, indicating minimal stiffness effects. The amplitude spectrum for PT1 located 0.05*l* from the fixed end is nearly identical to that of the bare plate, confirming negligible influence on the global dynamic response. Temperature compensation for the pressure sensor typically addresses static effects rather than dynamic thermal transients. Although we did not specifically test for the impact of thermal transients during sudden sensor immersion, no irregularities in sensor readings were observed during calibrations or tests, suggesting minimal influence. Nonetheless, this remains an important consideration for future research. The high-speed Phantom LAB340 camera, equipped with a Tokina AT-X Pro Macro 100 mm lens, is positioned perpendicular to the plate to capture both the breaking crest shape and plate strain. The camera delivers high-resolution images (1600 × 2560 pixels) with minimal distortion at a frame rate of 200 f.p.s. The field of view measures 30.39 cm × 48.63 cm, as shown in [figure 2\(c\)](#), encompassing the entire vertical plate and the approaching wave crest throughout the measurements. Plate deflection is quantified through an image processing routine that analyses each frame of the high-speed recordings. The process involves grey-scale conversion and thresholding to isolate the black plate tip, followed by centroid detection to track the tip displacement.

2.3. Laboratory procedure

The wavemaker, WGs, PTs and high-speed camera are synchronised by a data acquisition system. For each test, the wavemaker triggers the WG and PT recordings immediately. The high-speed camera is triggered by the wavemaker after a predetermined time, which can skip unnecessary image recordings before the wave crest enters the field of view. The acoustic Doppler velocimeter is triggered manually when the wavemaker is started. The velocity measurements across test repetitions are synchronised by analysing wave arrival times to diminish timing discrepancies. After the impact, the flume is left to settle for at least 30 minutes before the next test to minimise the effect of residual motions (Raby *et al.* 2022). To minimise the interference of the PT on the dynamic response of the elastic plate, only PT1 is installed during structural displacement measurements, and a single PT is used per run for pressure measurements at the ten designated points. Therefore, each wave condition is repeated at least 20 times. [Figure 3](#) illustrates the repeated measurements of wave surface elevation, flow velocity and impact pressure on the elastic plate for test 4. The results from two runs exhibit low standard deviations, particularly for the normalised wave surface elevations, which have a root mean square error (RMSE) below 0.03, and normalised flow velocities with an RMSE below 0.003. These findings highlight the wavemaker's capability to generate highly repeatable solitary wave impacts. Although the normalised impact pressure, $P/\rho gH$ (where ρ is the water density), shows slightly weaker repeatability, its RMSE remains below 0.3. All RMSE values reported here are non-dimensional, as they are computed based on normalised quantities. Consistent with these findings, experiments by Sou, Wu & Liu (2023) conducted in the same facility under comparable conditions, including the wave

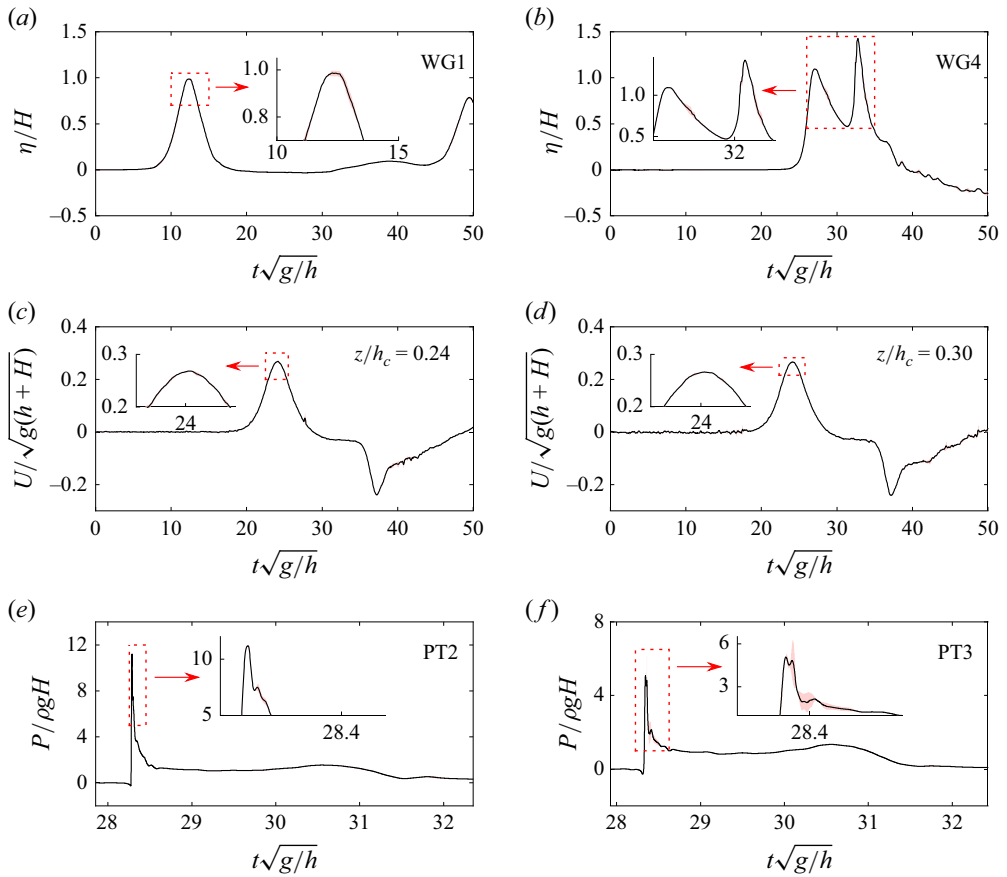


Figure 3. Repeated measurements of (a,b) wave surface elevation, (c,d) flow velocity and (e,f) pressure on the elastic plate for test 4. Coloured areas denote the standard deviations.

height, water depth and propagation distance, also demonstrated the excellent repeatability of the wavemaker.

2.4. Time series analysis

When a breaking wave impacts a vertical plate, the time series of pressure measurements $P(t)$ can be divided into three distinct phases (Bredmose *et al.* 2009). The initial impact phase is characterised by a sharp pressure spike reaching a maximum value P_{max} , as schematically illustrated in figure 4(a) for low-aeration impacts. In contrast, high-aeration impacts may result in sub-atmospheric pressures and subsequent pressure oscillations following the impact, as shown in figure 4 of Bullock *et al.* (2007). Finally, the post-impact phase is dominated by a smoother pressure distribution that closely resembles hydrostatic behaviour. While this phase is commonly referred to as ‘quasi-hydrostatic’, we emphasise that it may still include residual dynamic contributions, particularly due to wave diffraction and radiation effects interacting with the flexible plate. The pressure zero-crossing time, t_a , marks the impact start, while the end time, t_b , is defined as the point when the pressure falls below the maximum quasi-hydrostatic pressure, P_{hp} . Here, t_{max} represents the time at which the peak pressure occurs (Bullock *et al.* 2007). The central time t_0 (first standardised

Test no.	$t_a - t_0$ (ms)	$t_{max} - t_0$ (ms)	$t_b - t_0$ (ms)	P_J (Pa s)	$\Delta x_{imp}/l$	$\Delta x_{hp}/l$
1	—	—	—	0	0.000	0.006
2	−8.84	1.35	6.91	10.60	0.003	0.032
3	−17.95	7.05	7.60	14.62	0.009	0.050
4	−11.87	−8.62	16.03	45.57	0.028	0.078
5	−11.66	−10.01	17.39	68.75	0.048	0.101
6	−12.43	−11.33	20.97	103.76	0.065	0.112
7	−14.96	−6.36	23.59	184.26	0.095	0.145

Table 2. Summary of impact timestamps t_a , t_{max} , and t_b obtained from PT3, centred at t_0 , along with the corresponding pressure integrals and plate deflections. Here, $t_a - t_0$ and $t_b - t_0$ denote the start and end of the impact event, respectively, and the impact duration $t_b - t_a$ can be inferred accordingly.

pressure moment) of the impact time range is calculated by (Steer *et al.* 2021)

$$t_0 = \int_{t_a}^{t_b} (t - t_{max}) \tilde{P}(t) dt, \quad (2.1)$$

where t is the time and the tilde denotes the normalisation of the pressure time series by its integral $\tilde{P}(t) = P(t)/P_J$. Here, P_J represents the pressure integral over the impact duration, calculated using the trapezoidal method. To quantify the temporal spread of the impact, the temporal variance of the impact pressure is then parameterised (Steer *et al.* 2021)

$$\sigma_P^2 = \int_{t_a}^{t_b} (t - t_0)^2 \tilde{P}(t) dt, \quad (2.2)$$

which provides a measure of how the impact duration is distributed around its mean occurrence time. The obtained t_0 and σ_P for impact pressure vary depending on the location of the PT. Table 2 summarises the extracted parameters from the measurement of PT3. The wave force is estimated by integrating the pressure distribution over the plate under 2-D idealisation, with linear interpolation applied between pressure measurement points. The impulse I_{imp} per unit width is then obtained by integrating the force values over the impact time range

$$I_{imp} = \int_0^l P_J dz. \quad (2.3)$$

The time series of plate displacement at the free top is schematically represented in figure 4(b). The plate response can be interpreted as a two-stage process: an initial impact phase that triggers the plate deflection, followed by a continued excitation phase driven by quasi-hydrostatic pressure as the wave continues to interact with the plate. Specifically, following an initial negative deflection, the plate undergoes a sharp positive displacement driven by the impulsive impact pressure, reaching a peak displacement Δx_{imp} shortly after the impact duration $t_b - t_a$. During the latter stage, the plate deflects further under the oscillatory quasi-hydrostatic pressure and reaches its maximum displacement, Δx_{hp} , under the maximum quasi-hydrostatic pressure P_{hp} , before transitioning into free vibration governed by its natural frequency and material damping (Kimmoun *et al.* 2009; Hu & Li 2023). During free vibration, the wave has already retreated, making its influence relatively minor compared with material damping, which predominantly governs the plate's response. The two characteristic displacement values, Δx_{imp} and Δx_{hp} , identified in the present study, are listed in table 2 and shown in figure 11. This decomposition

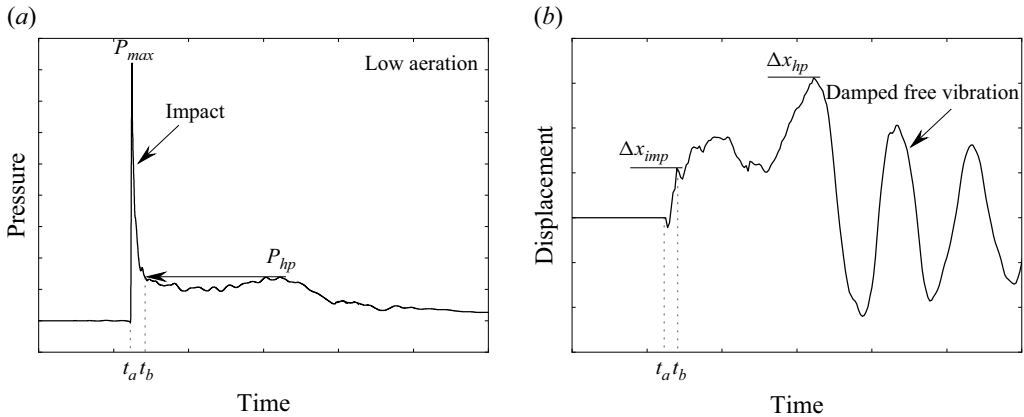


Figure 4. Schematic representations of breaking wave induced (a) pressure and (b) corresponding plate displacement at the free top.

highlights the transition from impulsive hydroelastic excitation to slower structural deformation under quasi-hydrostatic conditions, before the plate returns to free oscillation.

3. Results and discussion

The pressure characteristics and structural response in distinctive types of breaking wave impact on a vertical plate are presented in this section. Sections 3.1 and 3.2 describe the wave surface profiles, pressure measurements and plate response for four main impact types. Furthermore, § 3.3 discusses the effects of flexural rigidity on the key impact parameters. Building on these insights, § 3.4 presents and verifies the predictive law for plate deflections resulting from impact and maximum quasi-hydrostatic pressures. Finally, § 3.5 provides the uncertainty analysis.

3.1. Unbroken and slightly breaking

Tests in the unbroken and slightly breaking regimes exhibit almost no overturning wave crests and air entrapment. The approaching wave is either unbroken or marginally breaking on the plate surface, as shown in images of figure 5(a,c). The pressure time history of test 1 in the unbroken region shows only quasi-hydrostatic pressure on a long time scale, see figure 5(b). Since no impact event occurs, the central time t_0 is calculated by integrating the duration of quasi-hydrostatic pressure for this regime. Additionally, all parameters extracted from the impact region are zero. The plate's response appears quasi-static, with the plate stiffness balancing the external load and resulting in an almost in-phase relationship between pressure and deflection. The smallest measured plate deflection $\Delta x_{hp}/l = 0.006$ with a low acceleration of approximately 0.014 m s^{-2} is observed.

The slightly breaking impact for test 3 features appreciable sharp pressure with a low amplitude of $1.9\rho gH$ and relatively short duration of $0.16\sqrt{g/h}$, as seen in figure 5(d). The impact pressure maxima P_{max} is between 1.0 and 2.5 times the maximum quasi-hydrostatic pressure, which falls within the slightly breaking limit proposed by Bullock *et al.* (2007). Figure 7(a) presents the loading processes and associated pressure distributions imposed on the plate for test 3. The approaching wave front forces the run-up jet to rise rapidly at the plate. This can be found in figure 6(a) and the movie of test 3 in the supplementary material. The high impact pressure mainly concentrates below the strike point $z_{imp}/h = 0.177$. Afterward, the vertical jet with an acceleration of nearly $15g$

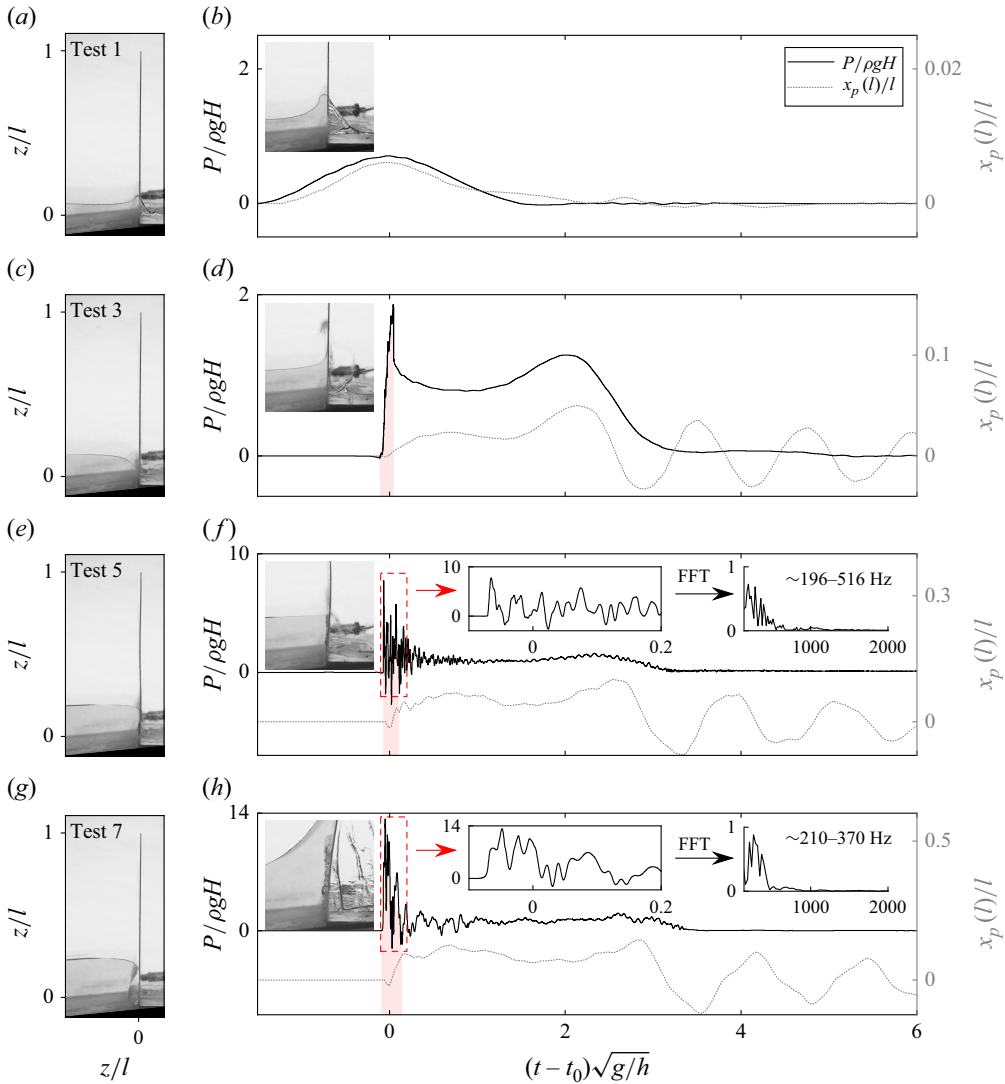


Figure 5. Selected time series of pressure (solid line) at PT3 and elastic plate displacement at the free top (dotted line). Each test is centred horizontally about its expected central time t_0 . Coloured areas denote the pressure impact time range defined in § 2.4. An enlarged view of pressure oscillations under aerated impacts is shown with the corresponding amplitude spectrum obtained via fast Fourier transform (FFT).

forms and induces a rapidly decreasing load along the plate, which is commonly observed in the ELPs introduced by Lafeber *et al.* (2012b). Finally, the quasi-hydrostatic pressure builds up and fades away following the wave drawdown process. To assess the nature of the pressure field after impact, we analyse the spatial distribution of the maximum quasi-hydrostatic pressure measured along the vertical plate. The term quasi-hydrostatic (Bullock *et al.* 2007; Bredmose *et al.* 2009) used in this study does not imply a purely hydrostatic pressure distribution, but rather refers to a pressure field that approximately follows a hydrostatic gradient while still allowing for residual dynamic contributions, such as those from wave diffraction, radiation and structural vibration. As illustrated in figure 7, the post-impact pressure profile exhibits a near-linear variation with depth for all tests,

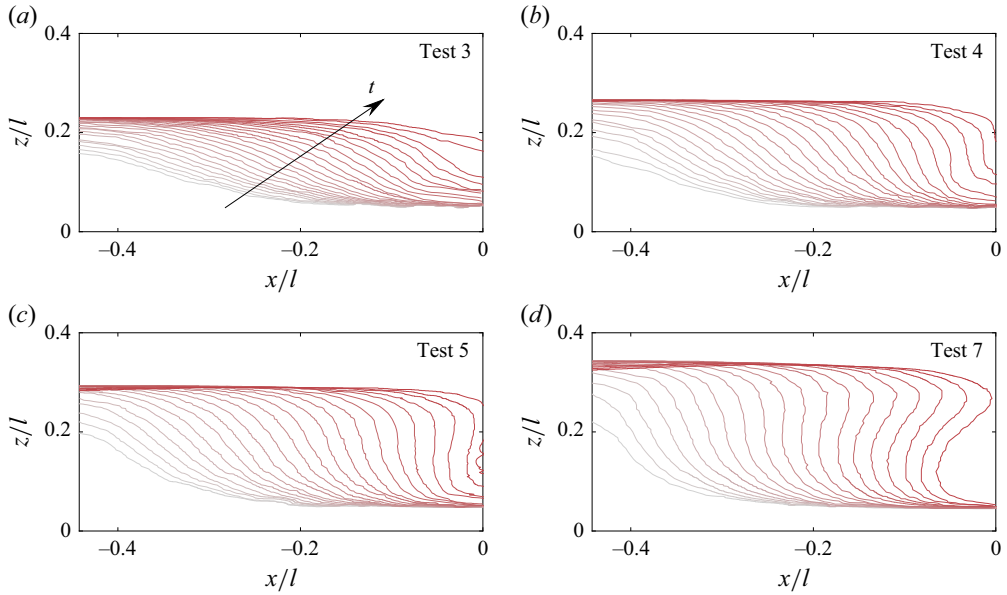


Figure 6. Selected instantaneous wave profile histories of (a) slightly breaking, (b) flip through, (c) low aeration and (d) high aeration. The time interval between successive profiles is 5 ms.

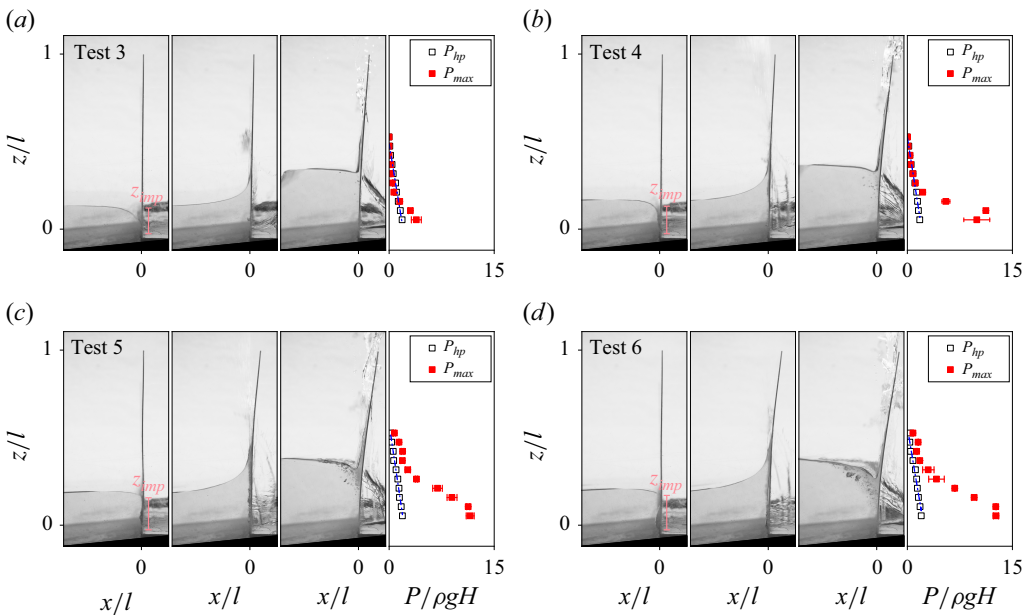


Figure 7. Images captured at key time stamps: incipient impact, Δx_{imp} and Δx_{hp} (from left to right) alongside pressure distributions along the vertical elastic plate for representative tests: (a) slightly breaking, (b) flip-through, (c) low-aeration and (d) high-aeration impacts. In the pressure plots, impact pressure maxima P_{max} are indicated by red solid squares, while the maximum quasi-hydrostatic pressures P_{hp} are shown as black open squares, fitted to a hydrostatic profile. Error bars represent measurement uncertainty, given by the standard deviation of the pressure readings.

which is characteristic of a hydrostatic distribution. Although some spatial fluctuations and dynamic effects remain, their influence becomes secondary, justifying the use of the term ‘quasi-hydrostatic’ to describe the dominant pressure trend in this phase. The relatively low pressure and small spatio-temporal extent of the slightly breaking impact naturally lead to an insignificant plate displacement. The plate deflection caused by the impact $\Delta x_{imp}/l$ is 0.009 with an acceleration of approximately 0.14 m s^{-2} , illustrated in [figure 5\(d\)](#). The plate deflects further with the increasing bending moment and reaches its maximum displacement of $\Delta x_{hp}/l = 0.05$ under the maximum quasi-hydrostatic pressure. The plate eventually vibrates freely with material damping at a frequency of $0.92 f_n$. The slight reduction in natural frequency is due to added mass effects in wet conditions.

3.2. Low and high aerations

The aerated impact on the plate is characterised by a distinct overturning wave crest accompanied by the run-up of the wave front, which can be found in [figure 6\(c,d\)](#) and movies of tests 5–7 in the supplementary material. The degree of the crest overturning determines the amount of air entrapment. The low-aeration impact experiences relatively little air enclosed by the wave front adjacent to the plate, as seen in [figure 5\(e\)](#) for test 5, while high aeration has an appreciable air-pocket entrainment between the plunging jet and plate prior to impact, as shown in [figure 5\(g\)](#) for test 7. Moreover, the flip-through impact (Peregrine 2003; Lugni *et al.* 2006) with a wave front almost parallel to the plate is observed in the surface profile history in [figure 6\(b\)](#) and the image in [figure 7\(b\)](#) for test 4, with little, if any, air entrapment. An arc with upward curvature forms between the wave crest and the run-up jet, gradually contracting to a point, as demonstrated in the movie of test 4 in the supplementary material. This process is similar to the ‘focusing surface’ phenomenon described by Wang *et al.* (2018). The rapidly focusing surface at the contact region leads to an upward splash with an acceleration of approximately 466 g close to 481 g observed in Wang *et al.* (2018). The pressure distribution along the plate exhibits the most spatially localised behaviour in all tests.

The pressure history of low aeration presents a shorter rise time and longer fall time compared with the slightly breaking impact, see [figure 5\(f\)](#) for test 5. The impact duration and pressure maxima significantly increase to $0.2\sqrt{g/h}$ and $8.9\rho gH$, respectively. The pressure oscillations during the impact process are associated with a dense cloud of bubbles formed by the fragmentation of the entrapped air pocket. When a wave impacts a vertical wall, the natural frequency f_b of an entrapped 2-D gas pocket with a semicircular cross-section of radius r in water can be estimated using the theoretical expression (Faltinsen & Timokha 2009, p. 499)

$$f_b = \frac{1}{2\pi} \sqrt{\frac{2\gamma P_0 \left(1 + \frac{1}{2}\lambda_d^2 r^2\right)}{\rho r^2 \left[\log\left(\frac{1}{2}\lambda_d r \tan \lambda_d d_b\right) + \frac{1}{4}\lambda_d^2 r^2\right]}}, \quad (3.1)$$

where $\gamma = 1.4$ is the ratio of specific heats for air, P_0 is the atmospheric pressure and

$$\lambda_d = \frac{\pi}{2(d_a + d_b)}, \quad (3.2)$$

where d_b and d_a represent the distances from the centre of the gas pocket to the free surface and the bottom boundary, respectively. These distances can be determined based on the bubble locations near the PT. This formulation accounts for boundary effects and better reflects the hydrodynamic conditions of low-aeration scenarios near solid walls. The bubble radii, identified from images in [figure 5\(f\)](#), range from approximately 2.5 to 7.5

mm, yielding a natural frequency between 195 and 517 Hz as estimated by (3.1). This range aligns well with the pressure oscillation frequencies obtained from the Fourier analysis of the pressure history after the impact peak. While FFT is limited in resolving transient signals, it is employed here in a complementary manner to identify dominant frequency content associated with the bubble dynamics. For this case with more pronounced impact characteristics, the plate response exhibits a distinct two-stage process, as illustrated in figure 4(b). The plate deflects to $\Delta x_{imp}/l = 0.048$ with an acceleration of 0.55 m s^{-2} due to the high impact pressure and long duration of test 5. High-frequency vibrations are observed, accompanied by pressure oscillations. The falling droplets during wave run-down also contribute to the plate deflection, as shown in figure 7(c). The impact pressure along the plate becomes less confined as the presence of air extends the impact zone. Following the maximum deflection $\Delta x_{hp}/l = 0.101$, the elastic plate vibrates at a frequency of $0.93 f_n$.

The pressure history of high aeration shows the measured highest pressure of $13.8\rho gH$ and longest duration of $0.24\sqrt{g/h}$ in all tests, see figure 5(h) for test 7. The negative (sub-atmospheric) pressure due to the trapped air expansion (Bullock *et al.* 2007; Steer *et al.* 2021) is not obvious herein because of the negligible air compressibility (Mach number $Ma \ll 0.3$) and air leakage effects as will be discussed in § 3.5. The image from test 7 shows a large air pocket breaking into a cluster of bubbles that move along with the vertical jet upon wave impact, as also observed in figure 7(d) for test 6. The bubbles generated from the fragmentation of the initial air pocket contribute to high-frequency pressure oscillations (210–370 Hz) even during high-aeration impacts. However, the oscillation frequency is lower than in low-aeration impacts due to the increased bubble radii. Note that the excited plate modes cause an elongated air cavity to form beneath the jet tongue following the impact shown in figure 7(d), which may influence the integrity of the structures involved. During the drawdown phase, the increase in kinetic energy (reflected in dynamic pressure) causes the measured pressure to slightly deviate from the hydrostatic assumption. In addition, the spatial extent of the impact pressure along the elastic plate further increases, similar to wave impacts on rigid structures (Bredmose *et al.* 2009). The plate deflection of test 7 reaches a maximum of $\Delta x_{imp}/l = 0.095$ with an acceleration of 1.73 m s^{-2} during the impact and $\Delta x_{hp}/l = 0.145$ under the maximum quasi-hydrostatic force, as shown in figure 5(h). Finally, the elastic plate vibrates at a frequency of $0.94 f_n$.

3.3. Effects of flexural rigidity

We have presented pressure characteristics and structural responses for an elastic plate under multimodal breaking wave impacts in §§ 3.1 and 3.2. On the fluid side, how hydroelasticity in turn influences impact pressure is debated. For isolated breaking wave impacts, previous laboratory experiments have shown that structural elasticity can reduce peak pressure (Mai *et al.* 2020). However, Shen *et al.* (2024) reported that elasticity has little influence on the impact load but modifies the impact duration and impulse. Attili, Heller & Triantafyllou (2023) indicated that the flexible plate does not necessarily lead to a smaller wave force compared with the rigid one. For impacts induced by successive wave breaking, Hu & Li (2023) showed that the impact variability caused by hydroelasticity is mainly due to the changes in wave crest shape caused by different residual motions between rigid and flexible structures, e.g. wave reflections and turbulence left from the preceding wave.

Figure 9 compares the maximum impact and quasi-hydrostatic pressure between rigid and elastic plates. The flexural rigidity EI of the rigid plate is approximately 300 times that of the elastic plate. The pressure coefficient C_p derived from the impact pressure

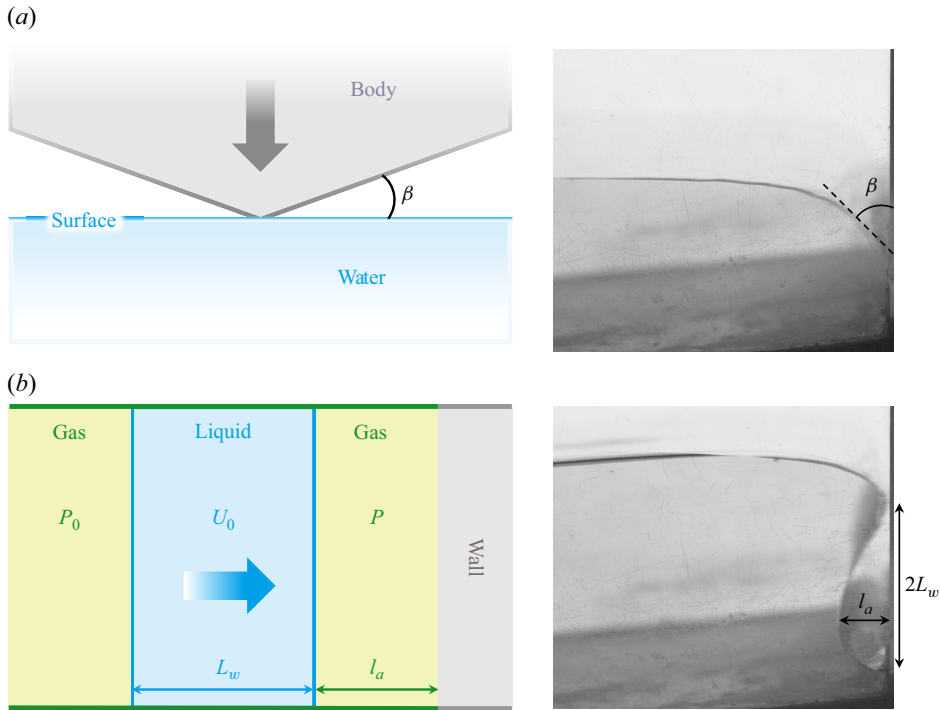


Figure 8. Illustration of the (a) 2-D Wagner model (ELP2) and (b) 1-D Bagnold solution (ELP3).

maxima $P_{max} = (1/2)\rho C_p U_0^2$ is depicted in figure 9(a). The wave front velocity U_0 is estimated from the high-speed video recordings using a cross-correlation algorithm for image analysis (Raffel *et al.* 2018), which tracks the displacement of the wave front between successive frames before impact. The accuracy of this method depends on the frame rate, resolution and visual contrast in the video. Under our experimental conditions, the uncertainty in U_0 is estimated to be within $\pm 5\%$. It is observed that C_p increases with H/h for the slightly breaking regime. Given that the flexural rigidity of the plate had negligible effects on the measured impact pressure, the model proposed by Wagner (1932) for a 2-D rigid wedge provides an estimate of the pressure coefficient

$$C_p = \frac{\pi^2}{4 \tan^2 \beta}, \quad (3.3)$$

where β represents the effective deadrise angle between the wetted and free surfaces, i.e. the angle between the wave front and vertical wall, as illustrated in figure 8(a) and listed in table 1. Here, C_p remains almost unchanged for aerated impacts, where the approaching fluid velocity U_0 mainly determines the impact pressure maxima. Using a one-dimensional (1-D) piston compressed air model to simplify the air-pocket phenomenon, the air cushion theory proposed by Bagnold (1939) provides an estimate of C_p within $\pm 10\%$ error for the aerated impacts under adiabatic conditions

$$P_{max} = 2.7 \frac{L_w}{l_a} \rho U_0^2, \quad (3.4)$$

where L_w is the length of the water column compressing the air, and l_a is the mean initial thickness of the air cushion, as displayed in figure 8(b) and listed in table 1. In accordance with Bagnold (1939) formulation, L_w is approximated as half the vertical width of the

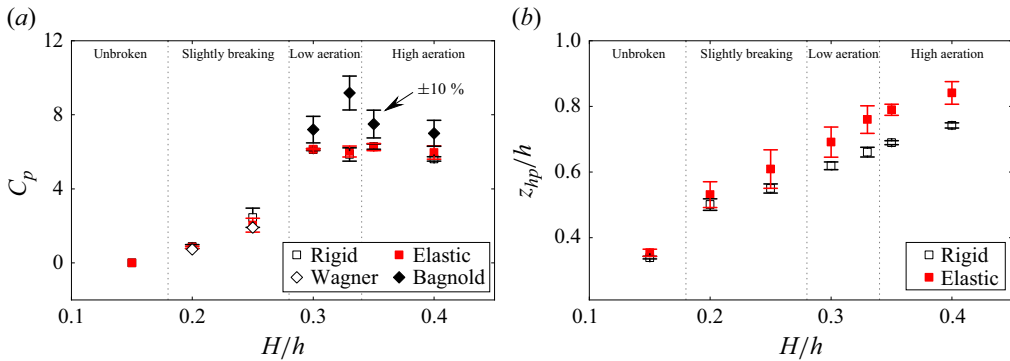


Figure 9. Breaking-wave-induced (a) pressure coefficient at the impact pressure maxima and (b) height of the water column corresponding to the maximum quasi-hydrostatic pressure on the rigid and elastic plates, where the error bars represent the pressure measurement uncertainty calculated as the standard deviation. The vertical dotted lines denote the boundaries separating the four distinctive impact types.

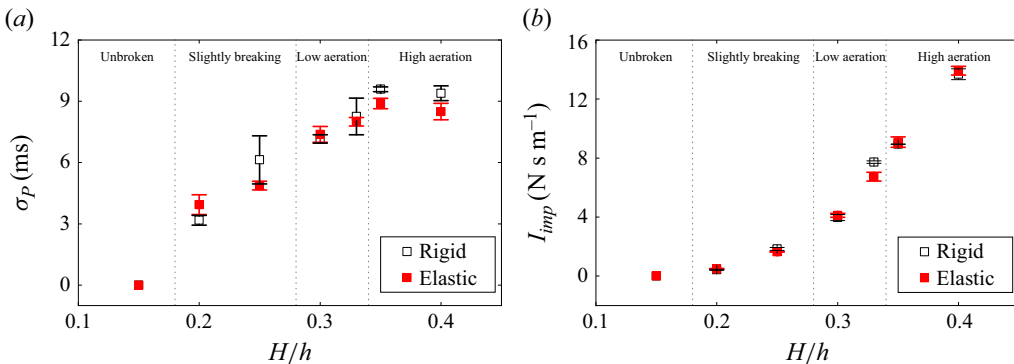


Figure 10. Breaking-wave-induced (a) temporal variance of impact pressure at PT3 and (b) impulse on the rigid and elastic plates, where the error bars represent the pressure measurement uncertainty calculated as the standard deviation. The vertical dotted lines denote the boundaries separating the four distinctive impact types.

air cushion, based on the rationale that the mass of water contributing to the impact is equivalent to that of a horizontal column with a cross-section equal to the frontal area of the cushion and a length equal to half the vertical cushion width. This estimation provides a practical way to quantify the water mass involved in the pressure generation mechanism. Wagner's model and Bagnold's theory give acceptable predictions for C_p in the present study, as shown by the diamond in figure 9(a). Note that C_p is indistinguishable between rigid and elastic plates, suggesting that the elasticity has little effect on the impact pressure maxima, which is also seen in Shen *et al.* (2024), who studied the performance of four materials with different Young's moduli under the flip-through impact.

The temporal deviation of impact pressure, σ_P , termed the characteristic impact duration, is shown in figure 10(a). The increase in aeration extends the impact duration σ_P . Consequently, the integrated impulse I_{imp} on the plate increases as the impact varies from slightly breaking to high aeration, as shown in figure 10(b). Likewise, the elasticity has little effect on the impact duration and impulse for distinctive breaking wave impact types. This observation is closely tied to the specific characteristics of the tested cantilever plate, whose relatively high stiffness and short structural response time result in minimal

deformation during the brief impact phase, as shown in [figure 5](#). The structural time scale is significantly longer than the fluid loading time scale, thereby reducing the dynamic amplification effects typically associated with hydroelastic impacts. However, it is also observed that the maximum quasi-hydrostatic pressure acting on the elastic plate is higher than that on the rigid plate, as shown by z_{hp} in [figure 9\(b\)](#). This is more pronounced for higher H/h because the increased deformation could create a convex shape to enhance the local run-up, which is also seen in a large-scale computational fluid dynamics simulation (Hu & Li 2023). This indicates that elasticity modifies the post-impact wave–structure interaction, potentially through radiation and diffraction effects during the longer-duration quasi-hydrostatic phase.

3.4. Predictive law for plate deflections

For hydroelastic impacts, the strains in the clamped-end plate are numerically determined using a beam model (Faltinsen & Timokha 2009, pp. 533–544). This study aims to develop a simplified predictive law for plate deflections following a breaking wave impact. The analysis relies on non-dimensional quantities derived from Euler–Bernoulli beam theory, assuming small deflections. The unsteady Euler–Bernoulli beam theory with constant flexural rigidity EI reads

$$\rho_s b \frac{\partial^2 x_p}{\partial t^2} + c_s \frac{\partial x_p}{\partial t} + EI \frac{\partial^4 x_p}{\partial z^4} = P. \quad (3.5)$$

The left-hand side describes the acceleration, damping and internal elastic forces per unit width of the plate, based on a beam model formulation. Here, x_p is the plate deflection relative to $x = 0$ m, c_s is the damping coefficient, E is Young’s modulus, $I = b^3/12$ is the moment of inertia and z is the vertical coordinate in the coordinate system ([figure 2](#)). The right-hand side describes the external distributed pressure.

The boundary conditions for the fixed bottom end on $z = 0$ are

$$\left. \begin{aligned} \frac{\partial x_p}{\partial z} &= 0 \quad \text{on} \quad z = 0, \\ x_p &= 0 \quad \text{on} \quad z = 0, \end{aligned} \right\} \quad (3.6)$$

and for the free top on $z = l$ are

$$\left. \begin{aligned} \frac{\partial^2 x_p}{\partial z^2} &= 0 \quad \text{on} \quad z = l, \\ \frac{\partial^3 x_p}{\partial z^3} &= 0 \quad \text{on} \quad z = l. \end{aligned} \right\} \quad (3.7)$$

We begin with a few simplifying assumptions to derive a practical prediction law for the maximum deflection of the elastic plate under breaking wave impact. First, the time derivative of the plate deflection, $\partial x_p / \partial t$, is considered negligible at the moment the maximum deflection is reached. Given the relative stiffness of the plate, its response time is short, and the inertial effects are minor compared with the elastic restoring force. Accordingly, the maximum deflection can be reasonably approximated using a quasi-static approach, corresponding to the first peak in the transient response rather than a fully static equilibrium deflection. Second, the maximum impact pressure is assumed to be uniformly distributed over the impact zone. Although [figure 7](#) reveals some spatial variation in the impact pressure, particularly under flip-through impact scenarios. The assumption of pressure uniformity within the impact zone, analogous to the uniform

impact velocity assumption (Faltinsen & Timokha 2009, p. 497), although idealised, facilitates the development of a simplified and generalisable relationship for estimating plate deflection. Third, the spatial distribution of the maximum quasi-hydrostatic pressure is assumed to follow a hydrostatic distribution, which is supported by the observed spatio-temporal pressure distributions (see figure 7).

The high impact pressure remains localised and short in duration (~ 25 ms), see figures 5 and 7. The spatial extent of the impact zone is defined by the vertical coordinate of the impact point, denoted as z_{imp} , which is measured from the still water level. It is identified through inspection of the high-speed video recordings, as shown in figure 7. When water impacts a flat surface at a velocity U_0 , the induced plate deflection, Δx_{imp} , can be estimated by assuming the external load corresponds to the pressure maxima, $P_{max} = (1/2)\rho C_p U_0^2$, within the impact zone

$$P = \begin{cases} \frac{1}{2}\rho C_p U_0^2, & z \leq z_{imp}, \\ 0, & z > z_{imp}, \end{cases} \quad (3.8)$$

where C_p is the pressure coefficient of the maximum impact pressure. After the impact, a quasi-hydrostatic pressure distribution is observed on the elastic plate, as shown in figure 7. While additional sensors at higher locations could provide further insights, the current set-up effectively captures the quasi-hydrostatic pressure distribution. Moreover, placing sensors higher up could influence the plate's response, as demonstrated in the impact hammer test. For the estimation of plate deflection under the maximum quasi-hydrostatic pressure, Δx_{hp} , the external load can be expressed as the hydrostatic pressure $P = \rho g(z_{hp} - z)$ over the fluid–solid interface

$$P = \begin{cases} \rho g(z_{hp} - z), & z \leq z_{hp}, \\ 0, & z > z_{hp}, \end{cases} \quad (3.9)$$

where z_{hp} is the height of the water column obtained by linearly fitting the measured maximum quasi-hydrostatic pressure from all pressure sensors, assuming a hydrostatic pressure distribution.

Substituting the above boundary conditions (3.6)–(3.9) to (3.5) can yield the plate displacements caused by the impact and maximum quasi-hydrostatic pressure, respectively. The maximum plate deflections at the free top $z = l$ induced by the impact and the maximum quasi-hydrostatic pressure are given as

$$\Delta x_{imp} = \frac{\rho C_p U_0^2 z_{imp}^3 (4l - z_{imp})}{48EI}, \quad (3.10a)$$

$$\Delta x_{hp} = \frac{\rho g z_{hp}^4 (5l - z_{hp})}{120EI}. \quad (3.10b)$$

Assuming $4l \gg z_{imp}$ and $5l \gg z_{hp}$, the plate deflection (3.10a,b) can be reduced to

$$\frac{\Delta x_{imp}}{l} \sim \frac{Ca_{imp}}{6}, \quad (3.11a)$$

$$\frac{\Delta x_{hp}}{l} \sim \frac{Ca_{hp}}{12}. \quad (3.11b)$$

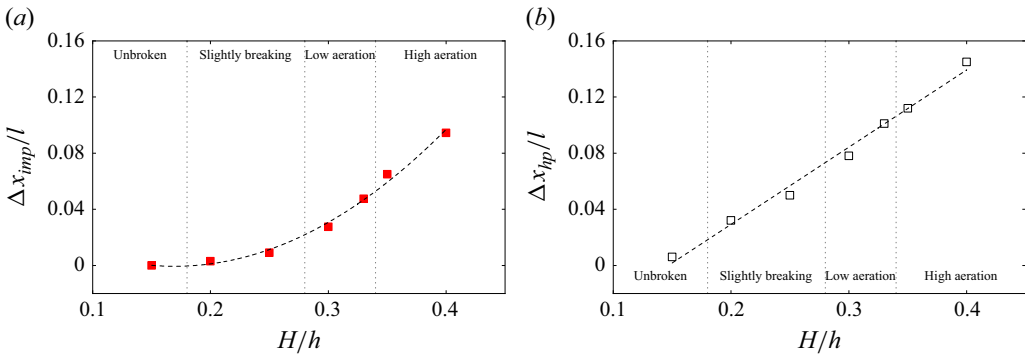


Figure 11. The plate deflections induced by (a) impact pressure with a parabolic best-fit curve and (b) maximum quasi-hydrostatic pressure with a linear best-fit line. The vertical dotted lines denote the boundaries separating the four distinctive impact types.

The deflections of the plate are essentially controlled by the Cauchy number defined in this study

$$Ca_{imp} = \frac{1}{2} \frac{\rho C_p U_0^2 z_{imp}^3}{EI}, \quad (3.12a)$$

$$Ca_{hp} = \frac{1}{2} \frac{\rho g z_{hp}^4}{EI}. \quad (3.12b)$$

The Cauchy number represents the relative magnitude of the fluid force and the restoring force due to structural stiffness. For constant EI , the impact Cauchy number Ca_{imp} is linearly related to the product of the impact pressure maxima and the cube of z_{imp} , while the quasi-hydrostatic Cauchy number Ca_{hp} is linearly correlated with the fourth power of z_{hp} . It is seen that both $\Delta x_{imp}/l$ and $\Delta x_{hp}/l$ are proportional to the Cauchy number. This predictive law will be verified in the following.

Figure 11 shows the plate deflections versus the initial wave height to water depth ratio H/h under different types of breaking wave impact. As the wave height increases from the unbroken to high-aeration range, the plate deflections induced by impact and maximum quasi-hydrostatic pressures tend to increase parabolically and linearly, respectively. The parabolic increase in $\Delta x_{imp}/l$ is because of the combination of increased impact spatial extent z_{imp} and pressure maxima P_{max} , as seen in figure 12(a,b). z_{imp} gradually increases with H/h in the impact regimes. In contrast, P_{max} shows strong sensitivity between slightly breaking and low aeration, which is aligned with a recent experimental study of breaking wave impacts on a monopile (Moalemi *et al.* 2024). The highest impact pressure, typically expected during low-aeration impact (Hattori *et al.* 1994; Jensen 2019), is instead observed in the high-aeration impact. This discrepancy may be attributed to the limited spatial resolution of the pressure measurements in this experiment, which may have failed to capture the localised peak pressure accurately. The impact Cauchy number Ca_{imp} then increases with H/h parabolically, as shown in figure 12(c). The predictive law (3.11a) for $\Delta x_{imp}/l$ presents satisfactory agreement against the measured values shown in figure 13(a). The linear fit with a slope of 0.87 in the dashed line suggests that $\Delta x_{imp}/l$ is slightly overpredicted due to the overestimation of the bending moment as we simplified the external load (3.8). Furthermore, the simplification from the plate deflection (3.10a) to the predictive law (3.11a) leads to an overestimation by 3 % to 5 % for the conditions studied.

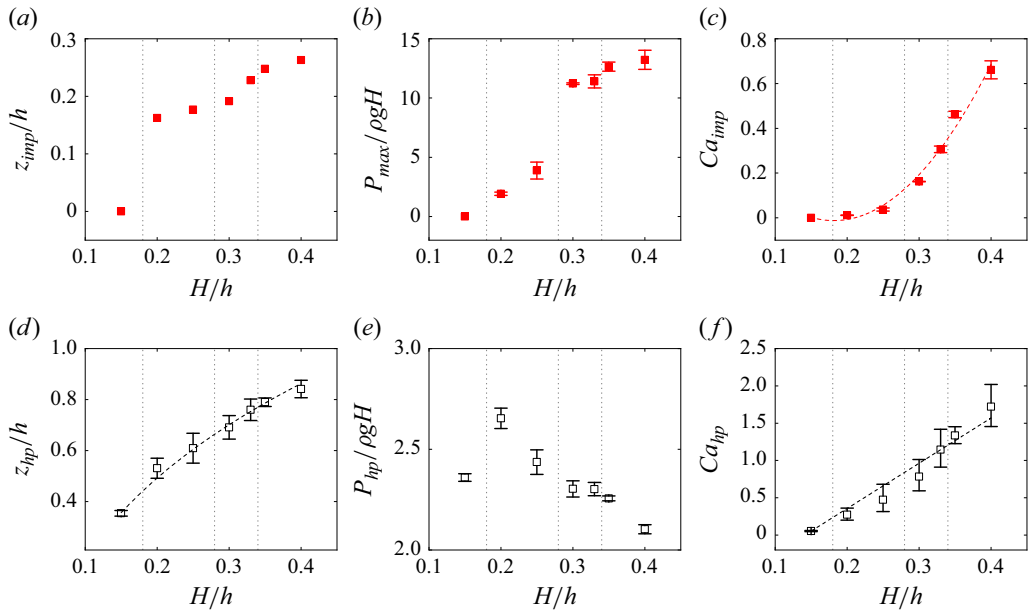


Figure 12. Impact pressure, maximum quasi-hydrostatic pressure and corresponding Cauchy number. (a) Spatial extent of the impact zone captured from the high-speed movie recordings, (b) impact pressure maxima and (c) impact Cauchy number with a parabolic best-fit curve. (d) Height of the water column with a quarter-power function fit, (e) maximum quasi-hydrostatic pressure and (f) quasi-hydrostatic Cauchy number with a linear best-fit line. The error bars represent the pressure measurement uncertainty calculated as the standard deviation. The vertical dotted lines denote the boundaries separating the four distinctive impact types.

Figure 12(d,e) displays the maximum quasi-hydrostatic pressure P_{hp} and corresponding height of the water column z_{hp} . Here, z_{hp} conforms to a quarter-power law with respect to H/h . Accordingly, the normalised P_{hp} gradually decreases with H/h from slightly breaking to high aeration. The quarter-power law suggests the linear relationship between the quasi-hydrostatic Cauchy number Ca_{hp} and H/h as well, according to the definition (3.12b), as presented in figure 12(f). The predictive law (3.11b) for $\Delta x_{hp}/l$ agrees well with the measured values, as shown in figure 13(b). The linear fit has a slope of 1.05, indicating $\Delta x_{hp}/l$ is slightly underpredicted due to the abovementioned pressure deviation from the hydrostatic assumption. The dynamic pressure, which is neglected in the simplification of the quasi-hydrostatic pressure, can also contribute to the deflection of the elastic plate.

3.5. Error and uncertainty

In all tests, the elastic plate considered upright slightly tilts toward the shore by 0.35° at the initial position, as seen in figure 2(c). The tiny plate tilt may cause a minor increase in the shear internal force $EI(\partial^4 x_p/\partial z^4)$ in the plate-normal direction, leading to a slightly underestimated plate displacement, especially for the plate response under a relatively lower impact impulse. Throughout this experimental campaign, the pressure measurements along the plate were conducted at least twice via the single transducer. The standard deviation across different runs for each impact is calculated to represent the pressure measurement uncertainty in §§ 3.1–3.4. The low deviation indicates that isolated impacts are reproducible, unlike successive wave breaking, which is shown to have significantly varying impact behaviour under nominally identical conditions (Bullock *et al.* 2007; Bredmose *et al.* 2009). To allow the elastic plate to move freely under the

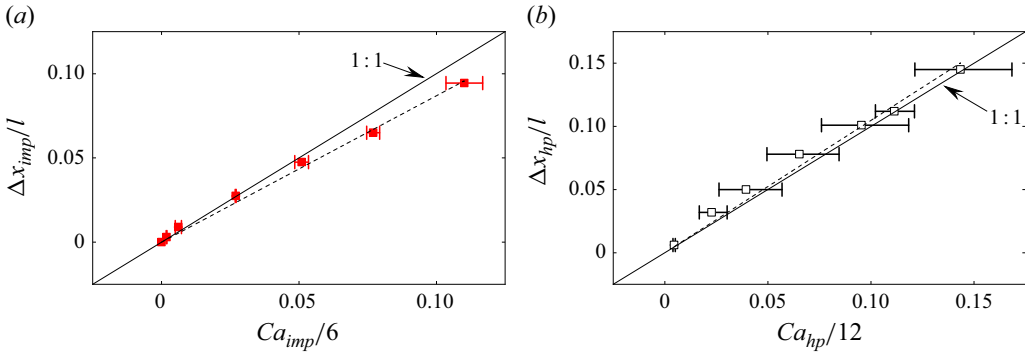


Figure 13. Plate deflection predictions: (a) $\Delta x_{imp}/l$ versus $Ca_{imp}/6$ linearly fitted with a zero intercept and (b) $\Delta x_{hp}/l$ versus $Ca_{hp}/12$ linearly fitted with a zero intercept. The error bars represent the pressure measurement uncertainty calculated as the standard deviation. The dashed line is the linear regression, and the solid line is the 1 : 1 line.

impact of breaking waves, we have preset a narrow gap of approximately 2.5 mm between both sides of the plate and the side walls of the flume. The gap in the 3-D nature of laboratory experiments allows the entrapped air to escape along the sides of the plate (Steer *et al.* 2021), which potentially results in less air compression/expansion and faster decay of pressure oscillations compared with vertical wall impacts (Hattori *et al.* 1994; Bullock *et al.* 2007; Hu & Li 2023). Additionally, water flowing through gaps depicted in the images of figure 7 inevitably reduces plate deflection, especially under the maximum quasi-hydrostatic pressure. Finally, the current set-up focuses on a 2-D analysis, with PTs aligned along a single vertical plane, limiting the ability to capture lateral pressure variations and 3-D effects such as irregular wave breaking and oblique impacts. To overcome these limitations, future research should incorporate advanced measurement techniques, such as multi-plane pressure arrays and volumetric particle image velocimetry, to enhance the understanding of 3-D hydroelasticity in breaking wave impacts.

4. Conclusions

This study experimentally investigates the hydroelastic response of a vertical cantilever plate subjected to a practical range of breaking wave impacts from non-breaking to highly aerated conditions. The observed response indicates that the initial deformation is primarily driven by impulsive hydrodynamic loading, while the subsequent quasi-static deflection arises from the water pile-up on the offshore side of the plate. The scaling relationships derived in this study suggest that both deformation phases consistently scale with the Cauchy number across different impact regimes.

Aeration is found to play a critical role in shaping hydroelastic impacts. The spatio-temporal extent of pressure on the plate increases with air entrapment between the wave crest and structure. During impacts, pressure oscillations linked to bubble dynamics are observed, especially under low-aeration conditions, resulting in high-frequency structural vibrations. The flip-through impact produces the most spatially concentrated pressure distribution and generates vertical splash jets with accelerations exceeding 450 g. Elasticity has a limited effect on peak pressure, impact duration and impulse within the tested conditions but leads to higher quasi-hydrostatic pressures compared with the rigid plate. These findings underscore the influence of relative time scales in assessing hydroelastic behaviour. While specific to the current structural set-up, they offer key insights into how flexibility alters wave-induced loading. Caution is warranted when generalising to

structures with different boundary conditions or flexural characteristics. The pressure coefficient at the impact peak increases with H/h in the slightly breaking regime and stabilises in aerated conditions. Classical models by Wagner and Bagnold provide reasonable estimates of peak pressures. The overall impulse gradually increases from slightly breaking to high-aeration wave impacts.

We propose and validate a predictive law for structural deflection under breaking wave impacts. The spatial extent of the impact zone z_{imp} and normalised pressure maxima P_{max} both increase with H/h , with P_{max} exhibiting strong sensitivity between slightly breaking and low-aeration transitions. The height corresponding to maximum quasi-hydrostatic pressure, z_{hp} , follows a quarter-power law with respect to H/h . Two distinct deflection stages are identified: a high-acceleration deflection Δx_{imp} during impact, and a high-magnitude deflection Δx_{hp} driven by quasi-hydrostatic loading. Both follow Cauchy number scaling: $\Delta x_{imp}/l \sim Ca_{imp}/6$ and $\Delta x_{hp}/l \sim Ca_{hp}/12$, with Δx_{imp} increasing parabolically and Δx_{hp} linearly with H/h .

While this study focuses on a single plate configuration, the set-up captures essential physics governing wave-structure interactions, particularly the transition between impulsive and quasi-static response. Although exploring broader ranges of flexibility would deepen understanding, reducing stiffness introduces experimental challenges. Future work could extend these findings through high-fidelity numerical modelling or experiments with variable stiffness and boundary conditions. The present results provide a valuable benchmark and enhance our understanding of hydroelastic effects in breaking wave impacts, with implications for coastal and offshore engineering applications.

Supplementary movies. Supplementary movies are available at <https://doi.org/10.1017/jfm.2025.10397>.

Acknowledgements. The first author thanks Dr W. Chen and Dr L. Yue for their helpful advice, and Dr Y. Wang and Dr X. Liao for their guidance on the wavemaker and pressure transducer. We would also like to thank three anonymous reviewers for their constructive suggestions.

Funding. This research is supported by the Ministry of Education, Singapore, under the MOE AcRF Tier 2 project POSEIDON: Predicting cOaStal brEakIng waves with advanced Data-driven turbulence mOdelliNg.

Declaration of interests. The authors report no conflict of interest.

REFERENCES

- ATTILI, T., HELLER, V. & TRIANTAFYLLOU, S. 2023 Wave impact on rigid and flexible plates. *Coast. Engng* **182**, 104302.
- BAGNOLD, R.A. 1939 Interim report on wave-pressure research. *J. Inst. Civil Engrs. Lond.* **12** (7), 202–226.
- BANNER, M.L. & PEREGRINE, D.H. 1993 Wave breaking in deep water. *Annu. Rev. Fluid Mech.* **25** (1), 373–397.
- BREDMOSE, H., BULLOCK, G.N. & HOGG, A.J. 2015 Violent breaking wave impacts. Part 3. Effects of scale and aeration. *J. Fluid Mech.* **765**, 82–113.
- BREDMOSE, H., PEREGRINE, D.H. & BULLOCK, G.N. 2009 Violent breaking wave impacts. Part 2: modelling the effect of air. *J. Fluid Mech.* **641**, 389–430.
- BULLOCK, G.N., OBHRAI, C., PEREGRINE, D.H. & BREDMOSE, H. 2007 Violent breaking wave impacts. Part 1: Results from large-scale regular wave tests on vertical and sloping walls. *Coast. Engng* **54** (8), 602–617.
- CHAN, E.S. & MELVILLE, W.K. 1988 Deep-water plunging wave pressures on a vertical plane wall. *Proc. R. Soc. Lond. A* **417** (1852), 95–131.
- COOKER, M.J. & PEREGRINE, D.H. 1990 Violent water motion at breaking-wave impact. In *Proceedings of the 22nd International Conference on Coastal Engineering*, pp. 164–176. American Society of Civil Engineering.
- COOKER, M.J. & PEREGRINE, D.H. 1995 Pressure-impulse theory for liquid impact problems. *J. Fluid Mech.* **297**, 193–214.

- DEANE, G.B. & STOKES, M.D. 2002 Scale dependence of bubble creation mechanisms in breaking waves. *Nature* **418** (6900), 839–844.
- DEIKE, L., MELVILLE, W.K. & POPINET, S. 2016 Air entrainment and bubble statistics in breaking waves. *J. Fluid Mech.* **801**, 91–129.
- DIAS, F. & GHIDAGLIA, J.-M. 2018 Slamming: recent progress in the evaluation of impact pressures. *Annu. Rev. Fluid Mech.* **50** (1), 243–273.
- EZETA, R., PALACIOS MUÑOZ, B., FAN, Y.L., KIM, N., COUTY, N., BROSSET, L. & VAN DER MEER, D. 2025 Large-scale wave impact of a boiling liquid. *J. Fluid Mech.* **1008**, A22.
- FALTINSEN, O.M. 2000 Hydroelastic slamming. *J. Mar. Sci. Technol.* **5** (2), 49–65.
- FALTINSEN, O.M. & TIMOKHA, A.N. 2009 *Sloshing*. Cambridge University Press.
- GRILLI, S.T., SVENDSEN, I.A. & SUBRAMANYA, R. 1997 Breaking criterion and characteristics for solitary waves on slopes. *J. Waterway Port Coastal Ocean Engng* **123** (3), 102–112.
- GRIMSHAW, R. 1971 The solitary wave in water of variable depth. Part 2. *J. Fluid Mech.* **46** (3), 611–622.
- HATTORI, M., ARAMI, A. & YUI, T. 1994 Wave impact pressure on vertical walls under breaking waves of various types. *Coast. Engng* **22** (1), 79–114.
- HERTERICH, J.G., COX, R. & DIAS, F. 2018 How does wave impact generate large boulders? Modelling hydraulic fracture of cliffs and shore platforms. *Mar. Geol.* **399**, 34–46.
- HU, Z., HUANG, L. & LI, Y. 2023 Fully-coupled hydroelastic modeling of a deformable wall in waves. *Coast. Engng* **179**, 104245.
- HU, Z. & LI, Y. 2023 Two-dimensional simulations of large-scale violent breaking wave impacts on a flexible wall. *Coast. Engng* **185**, 104370.
- HULL, P. & MÜLLER, G. 2002 An investigation of breaker heights, shapes and pressures. *Ocean Engng* **29** (1), 59–79.
- JENSEN, A. 2019 Solitary wave impact on a vertical wall. *Eur. J. Mech. B/Fluids* **73**, 69–74.
- KAPSENBERG, G.K. 2011 Slamming of ships: where are we now? *Phil. Trans. R. Soc. A* **369**, 2892–2919.
- KENNEDY, A.B., COX, R. & DIAS, F. 2021 Storm waves may be the source of some ‘tsunami’ coastal boulder deposits. *Geophys. Res. Lett.* **48** (11), e2020GL090775.
- KIMMOUN, O., MALENICA, Š & SCOLAN, Y.M. 2009 Fluid structure interactions occurring at a flexible vertical wall impacted by a breaking wave. In *The Nineteenth International Offshore and Polar Engineering Conference*, pp. 308–315. Osaka, Japan.
- LAFEBER, W., BOGAERT, H. & BROSSET, L. 2012a Comparison of wave impact tests at large and full scale: results from the Sloskel project. In *The Twenty-second International Offshore and Polar Engineering Conference*. International Society of Offshore and Polar Engineers.
- LAFEBER, W., BOGAERT, H. & BROSSET, L. 2012b Elementary Loading Processes (ELP) involved in breaking wave impacts: findings from the Sloskel project. In *The Twenty-second International Offshore and Polar Engineering Conference*. International Society of Offshore and Polar Engineers.
- LI, Y. & FUHRMAN, D.R. 2021 Computational fluid dynamics simulation of deep-water wave instabilities involving wave breaking. *J. Offshore Mech. Arctic Engng* **144** (2), 021901.
- LI, Y. & FUHRMAN, D.R. 2022 On the turbulence modelling of waves breaking on a vertical pile. *J. Fluid Mech.* **953**, A3.
- LI, Y., LARSEN, B.E. & FUHRMAN, D.R. 2022 Reynolds stress turbulence modelling of surf zone breaking waves. *J. Fluid Mech.* **937**, A7.
- LUGNI, C., BROCCINI, M. & FALTINSEN, O.M. 2006 Wave impact loads: the role of the flip-through. *Phys. Fluids* **18** (12), 122101.
- MAI, T., MAI, C., RABY, A. & GREAVES, D.M. 2020 Hydroelasticity effects on water-structure impacts. *Exp. Fluids* **61** (9), 1–19.
- VAN MEERKERK, M., POELMA, C., HOFLAND, B. & WESTERWEEL, J. 2022 Gas flow dynamics over a plunging breaking wave prior to impact on a vertical wall. *Eur. J. Mech. B/Fluids* **91**, 52–65.
- MELVILLE, W.K. 1982 The instability and breaking of deep-water waves. *J. Fluid Mech.* **115**, 165–185.
- MOALEMI, A., BREDMOSE, H., KRISTIANSEN, T. & PIERELLA, F. 2024 Wave front perturbation effect on the variability of monopile wave impact loads. *J. Fluid Mech.* **984**, A65.
- OUMERACI, H. 1994 Review and analysis of vertical breakwater failures — lessons learned. *Coast. Engng* **22** (1), 3–29.
- PEREGRINE, D.H. 1983 Breaking waves on beaches. *Annu. Rev. Fluid Mech.* **15** (1), 149–178.
- PEREGRINE, D.H. 2003 Water-wave impact on walls. *Annu. Rev. Fluid Mech.* **35** (1), 23–43.
- PEREGRINE, D.H. & THAIS, L. 1996 The effect of entrained air in violent water wave impacts. *J. Fluid Mech.* **325**, 377–397.
- PLESSET, M.S. & PROSPERETTI, A. 1977 Bubble dynamics and cavitation. *Annu. Rev. Fluid Mech.* **9** (1), 145–185.

- QING, J., LIU, J. & GUO, A. 2024 Experimental study on focused wave breaking on an inclined plate. *Ocean Engng* **304**, 117892.
- RABY, A., BULLOCK, G., JONATHAN, P., RANDELL, D. & WHITTAKER, C. 2022 On wave impact pressure variability. *Coast. Engng* **177**, 104168.
- RAFFEL, M., WILLERT, C.E., SCARANO, F., KÄHLER, C.J., WERELEY, S.T. & KOMPENHANS, J. 2018 *Particle Image Velocimetry: A Practical Guide*. Springer.
- SHEN, L., WEI, Z., JI, S. & ZHANG, D. 2024 Experimental study of liquid slamming in elastic rectangular tanks under the flip-through impact. *Mar. Struct.* **94**, 103550.
- SOU, I.M., WU, Y.-T. & LIU, P.L.F. 2023 Swash flows generated by a train of solitary waves on a planar slope. *J. Fluid Mech.* **968**, A1.
- SRIRAM, V. & MA, Q.W. 2012 Improved MLPG_R method for simulating 2D interaction between violent waves and elastic structures. *J. Comput. Phys.* **231** (22), 7650–7670.
- STEER, J.N., KIMMOUN, O. & DIAS, F. 2021 Breaking-wave induced pressure and acceleration on a cliff-top boulder. *J. Fluid Mech.* **929**, R1.
- TEN, I., MALENICA, Š. & KOROBKIN, A. 2011 Semi-analytical models of hydroelastic sloshing impact in tanks of liquefied natural gas vessels. *Phil. Trans. R. Soc. A* **369** (1947), 2920–2941.
- THOMPSON, C.F., YOUNG, A.P. & DICKSON, M.E. 2019 Wave impacts on coastal cliffs: do bigger waves drive greater ground motion? *Earth Surf. Process. Landf.* **44** (14), 2849–2860.
- TIRON, R., MALLON, F., DIAS, F. & REYNAUD, E.G. 2015 The challenging life of wave energy devices at sea: a few points to consider. *Renew. Sustain. Energy Rev.* **43**, 1263–1272.
- TOPLISS, M.E., COOKER, M.J. & PEREGRINE, D.H. 1992 Pressure oscillations during wave impact on vertical walls. In *Proceedings of the 23rd International Conference on Coastal Engineering*, pp. 1639–1650. American Society of Civil Engineering.
- WAGNER, H. 1932 Über stoß- und gleitvorgänge an der oberfläche von flüssigkeiten. *Z. Angew. Math. Mech.* **12** (4), 193–215.
- WANG, A., IKEDA-GILBERT, C.M., DUNCAN, J.H., LATHROP, D.P., COOKER, M.J. & FULLERTON, A.M. 2018 The impact of a deep-water plunging breaker on a wall with its bottom edge close to the mean water surface. *J. Fluid Mech.* **843**, 680–721.
- WEI, Y., ABADIE, T., HENRY, A. & DIAS, F. 2016 Wave interaction with an oscillating wave surge converter. Part II: Slamming. *Ocean Engng* **113**, 319–334.
- YOUNG, W.C., BUDYNAS, R.G. & SADEGH, ALI M. 2012 *Roark's Formulas for Stress and Strain*. McGraw-Hill Education.